FEBS Open Bio 3 (2013) 496–504

journal homepage: www.elsevier.com/locate/febsopenbio

# Crystal structures of *Phanerochaete chrysosporium* pyranose 2-oxidase suggest that the N-terminus acts as a propeptide that assists in homotetramer assembly

Noor Hassan[a], Tien-Chye Tan[b], Oliver Spadiut[a], Ines Pisanelli[c], Laura Fusco[c], Dietmar Haltrich[c], Clemens K. Peterbauer[c], Christina Divne[a,b,*]

[a]KTH Royal Institute of Technology, School of Biotechnology, Albanova University Center, Roslagstullsbacken 21, S-10691 StockholmSweden
[b]Karolinska Institute, Department of Medical Biochemistry and Biophysics, Scheelelaboratoriet, Scheeles väg 2, S-17177 StockholmSweden
[c]BOKU University of Natural Resources and Life Sciences, Food Biotechnology Laboratory, A-1190 ViennaAustria

ARTICLE INFO

*Article history:*
Received 28 October 2013
Received in revised form 30 October 2013
Accepted 31 October 2013

*Keywords:*
Pyranose 2-oxidase
Propeptide
Oligomerization
Thermostability
Crystal structure
Lignin degradation

ABSTRACT

**The flavin-dependent homotetrameric enzyme pyranose 2-oxidase (P2O) is found mostly, but not exclusively, in lignocellulose-degrading fungi where it catalyzes the oxidation of β-D-glucose to the corresponding 2-keto sugar concomitantly with hydrogen peroxide formation during lignin solubilization. Here, we present crystal structures of P2O from the efficient lignocellulolytic basidiomycete *Phanerochaete chrysosporium*. Structures were determined of wild-type *Pc*P2O from the natural fungal source, and two variants of recombinant full-length *Pc*P2O, both in complex with the slow substrate 3-deoxy-3-fluoro-β-D-glucose. The active sites in *Pc*P2O and P2O from *Trametes multicolor* (*Tm*P2O) are highly conserved with identical substrate binding. Our structural analysis suggests that the 17 °C higher melting temperature of *Pc*P2O compared to *Tm*P2O is due to an increased number of intersubunit salt bridges. The structure of recombinant *Pc*P2O expressed with its natural N-terminal sequence, including a proposed propeptide segment, reveals that the first five residues of the propeptide intercalate at the interface between A and B subunits to form stabilizing, mainly hydrophobic, interactions. In the structure of mature *Pc*P2O purified from the natural source, the propeptide segment in subunit A has been replaced by a nearby loop in the B subunit. We propose that the propeptide in subunit A stabilizes the A/B interface of essential dimers in the homotetramer and that, upon maturation, it is replaced by the loop in the B subunit to form the mature subunit interface. This would imply that the propeptide segment of *Pc*P2O acts as an intramolecular chaperone for oligomerization at the A/B interface of the essential dimer.**



## 1. Introduction

The flavoprotein pyranose oxidase (P2O; EC 1.1.3.10) is found in most lignocellulolytic fungi [1–3] where it catalyzes the highly regioselective oxidation of D-glucose and generation of hydrogen peroxide as an integral part of the fungal degradative and metabolic machinery. Besides the general importance of P2O in wood decay and recycling, the enzyme is attracting interest based on its unusual mechanistic features and potential use in a wide range of applications, e.g., sugar biotransformation reactions, synthesis of rare sugars and fine chemicals [4], and in enzymatic biofuel cells [5].

P2O was first isolated from *Polyporus obtusus* [7], and later from additional wood-rotting fungi, including the highly efficient lignocellulose-degrading fungus *Phanerochaete chrysosporium* [9]. P2O from *P. chrysosporium* (*Pc*P2O) is expressed together with other redox-active enzymes when lignin is used as carbon source and displays similar regulation patterns, which strongly implies that the principal function lies in lignin solubilization [10]. The 270-kDa large enzyme is homotetrameric with a subunit molecular mass of 68 kDa where each of the four identical chains carries one active site and binding pocket for flavin adenine dinucleotide (FAD) [12]. Like other P2Os, *Pc*P2O catalyzes the oxidation of a number of aldopyranoses,

*Abbreviations:* *2F*Glc, 2-deoxy-2-fluoro-D-glucose; *3F*Glc, 3-deoxy-3-fluoro-D-glucose; DTT, dithiothreitol; HEPES, 4-(2-hydroxyethyl)-1-piperazineethanesulfonic acid; IMAC, by immobilized metal ion affinity chromatography; IPTG, β-D-1-thiogalactopyranoside; MES, 2-(*N*-morpholino) ethanesulfonic acid; MWCO, molecular weight cut off; P2O, pyranose oxidase; PBS, phosphate buffered saline; PDB, Protein Data Bank; PEG, polyethylene glycol; TEV, Tobacco Etch Virus.

* Corresponding author at: KTH Royal Institute of Technology, School of Biotechnology, Albanova University Center, Roslagstullsbacken 21, S-10691StockholmSweden. Tel.: +46 8 55378296; fax: +46 8 55378468.
*E-mail address:* divne@biotech.kth.se (C. Divne).

2211-5463 
http://dx.doi.org/10.1016/j.fob.2013.10.010

preferably glucopyranose, at the C2 position yielding the corresponding 2-keto sugars [13].

The related *Trametes multicolor* P2O (*Tm*P2O) has been shown to catalyze this reaction by a ping-pong type mechanism [14]. The overall reaction includes two half-reactions: a reductive half-reaction whereby β-D-Glc is oxidized at C2 to 2-keto-D-Glc [14], the flavin adenine dinucleotide (FAD) is reduced to $FADH_2$, and the keto sugar is released. The enzyme is highly regioselective catalyzing almost exclusively 2-oxidation of glucose [2,16–18]. Rare instances of C3 oxidation have been reported for some substrates [16]. The following oxidative half-reaction is pH-dependent [19], and involves the reduction of $O_2$ to $H_2O_2$ concomitantly with flavin re-oxidation. Oxygen activation during the oxidative half-reaction has been shown to involve a transient covalent flavin C(4a)-hydroperoxide intermediate [19]. P2O from *Peniophora gigantea* was observed to oxidize β-D-glucose at the C2 position, whereas 2-deoxy-D-glucopyranose was oxidized at the C3 position to yield 3-dehydroaldose (3-ketoaldose) [16]. This finding pinpointed an inherent ability of P2O to oxidize similar substrates at different positions, i.e., with different regioselectivity.

P2O has great potential in a variety of applications, including sugar biotransformation reactions, analytical tools, chemoenzymatic synthesis (reviewed in [4]), and in biosensors or biofuel cells.[5] For the most common electron-donor substrates, 2- to 3-fold higher specificity constants ($k_{cat}/K_m$) have been observed for *Pc*P2O compared with *Tm*P2O, and a similar trend is seen for common electron-acceptor substrates [21]. To be useful as a biocatalyst, an enzyme typically has to display considerable stability under operational conditions. In this context it is interesting to note that *Pc*P2O is significantly more thermostable ($T_m$ 75.4 °C) than the homologs from *Trametes multicolor* and *Lyophyllum shimeji* [21], which display $T_m$ values of 58.2 °C and 54.9 °C, respectively. Knowledge about the three-dimensional structure provides an important framework within which analysis of differences in thermostability can be discussed, and to suggest structural determinants to be targeted by mutagenesis to further fine tune catalytic and biophysical properties to meet the demands for industrial use in biocatalysis.

To date, crystal structures of P2O from only two fungal species have been reported, namely *Tm*P2O [22] and a P2O from *Peniophora* sp. [23]. Whereas the *Trametes* and *Peniophora* P2Os share 99.7% sequence identity with only two amino acids differing, the amino-acid sequence of *Pc*P2O [10] is distinctly different, especially in the N-terminal region, with only 40% overall sequence identity to the other two P2Os of known structure. To further elucidate how different P2Os differ at the structural level, and how differences are manifested at functional and mechanistic levels, crystal structures of *Pc*P2O from three different sources were resolved: the 1.80-Å structure of wild-type *Pc*P2O from the natural source *P. chrysosporium*; the 1.80-Å structure of recombinant wild-type *Pc*P2O (full-length gene coding for residues 1–621) expressed in *Escherichia coli* with a non-cleavable N-terminal T7-epitope tag; and the 2.40-Å structure of the *Pc*P2O variant H158A (full-length gene coding for residues 1–621) expressed with a cleavable hexahistidine tag that was removed proteolytically to yield the full-length gene product with an authentic N-terminus. The latter two crystal structures were determined in the presence of the slow substrate 3-deoxy-3-fluoro-β-D-glucose (3*F*Glc). Based on these structures, we compare *Pc*P2O with other P2Os of known structure with emphasis on thermal stability, and discuss the possibility of a propeptide functionality at the N-terminus.

## 2. Materials and methods

### 2.1. Production of wild-type PcP2Os

Wild-type *Pc*P2O from *P. chrysosporium* strain K-3 [24], referred to as $PcP2O_{NATWT}$, was produced in shake flask, and purified from mycelial extracts as previously described [3]. In brief, a combination of anion exchange and hydrophobic interaction chromatography was used to obtain an apparently homogenous enzyme preparation. The gene for *Pc*P2O (UNP Q6QWR1) coding for the 621 amino acid subunit of *Pc*P2O has been previously cloned into the bacterial expression vector pET21a( + ) carrying an N-terminal T7-epitope tag (coding for the amino-acid sequence $^{-14}$MASMTGGQQMGRGS$^{-1}$) where $^{-3}$RGS$^{-1}$ are additional cloning artifacts introduced by the restriction site, as well as a non-cleavable C-terminal hexahistidine tag (amino-acid sequence $^{622}$KLAAALEHHHHHH$^{634}$), and expressed in *E. coli* strain BL21 (DE3), and produced as reported earlier [12]. The recombinant wild-type variant is referred to as $PcP2O_{RECWT}$.

### 2.2. Cloning, expression and purification of PcP2O variant H158A ($PcP2O_{RECH158A}$)

To generate the *Pc*P2O mutant H158A, the *P. chrysosporium p2o* gene from the original vector [12] was subjected to site-directed mutagenesis using PCR. The template, pLF07, and the primers *Pc*P2O-H158A_fwd (5′-GGCATGAGCACTGCCTGGACGTGCGCAACC-3′), *Pc*P2O-H158A_rev (5′-GCTCATGCCCCCGACGCCGCGCGTGAC-3′) were used for mutagenic PCR reactions. The PCR reaction contained 2.5 U Pfu DNA polymerase (Fermentas, Germany), 100 ng of plasmid DNA, 5 pmol of each primer, 10 μM of each dNTP and 1 × PCR buffer (Fermentas) in a total volume of 50 μL. The following conditions were used for mutagenic PCRs: 95 °C for 4 min, then 30 cycles of 94 °C for 30 s; 65 °C for 30 s; 72 °C for 16 min, with a final incubation at 72 °C for 10 min. Following PCR, the methylated template-DNA was degraded by digestion with 10 U of *Dpn*I at 37 °C for 3 h. The remaining PCR products were separated by agarose gel electrophoresis and purified using the Wizard SV Gel and PCR-Clean-Up System (Promega, USA). PCR products (5 μL) were transformed into electro-competent *E. coli* BL21 Star DE3 cells. To prove that only the desired mutation had occurred, the mutated *Pc*P2O-encoding gene was sequenced by a commercial provider (VBC Biotech, Vienna, Austria) using primers T7prom_fwd (5′-AATACGACTCACTATAGGG-3′) and T7term_rev (5′-GCTAGTTATTGCTCAGCGG-3′).

The gene was amplified by standard PCR, and the insert cloned into the pNIC28-Bsa4 vector [25] using ligation-independent cloning [26]. The vector adds 23 residues comprising a hexahistidine ($His_6$) tag and a Tobacco Etch virus (TEV) protease cleavage site to the N-terminus of the expressed protein (sequence $^{-23}$MHHHHHHSSGVDLGTENLYFQSM$^{-1}$). Cleavage with TEV protease leaves the sequence $^{-2}$SM$^{-1}$ at the N-terminus. To reduce the number of additional N-terminal residues, the naturally occurring N-terminal methionine in the *pcp2o* gene was replaced by the translation start Met, leaving only an additional serine. The recombinant plasmid expressing $His_6$-TEV-*Pc*P2O was initially transformed into the *E. coli* cloning strain Mach1™ (Invitrogen) grown on Luria Bertani (LB) agar plates supplemented with 5% sucrose and 50 μg/mL kanamycin for the selection of recombinant plasmids with cleaved SacB (levansucrase).

Recombinant plasmids were isolated from Mach1 cells using plasmid preparation with the QIAprep® Spin Miniprep Kit (Qiagen), followed by plasmid transformation into the *E. coli* expression strain BL21(DE3). Transformed BL21(DE3) cells were grown in 0.6 L Terrific Broth (TB) medium supplemented with 50 mg/mL kanamycin, 60 mL glycerol (per 600 mL), 4 mM glucose, and 0.8 mM $MgSO_4$. The cultivation broth was inoculated with 7 mL overnight seed culture of BL21(DE3) and allowed to grow at 37 °C with constant shaking at 200 rpm until reaching an $OD_{600}$ of 0.7, at which *Pc*P2O expression was induced with 0.24 mM isopropyl β-D-1-thiogalactopyranoside (IPTG). The induced culture was grown for 18 h at 18 °C.

Cells were harvested by centrifugation at 4 °C (8983 *rcf*) using an Avanti J-20 XP centrifuge (Beckman) with rotor JLA 8.1000 for 15 min. The bacterial cell pellet was re-suspended in 3 volumes of lysis buffer

**Table 1**
Details of interactions between P2Os and 3-fluorinated glucose.

| | *Tm*P2O$_{RECH167A}$[a] | | *Pc*P2O$_{RECWT}$ | | *Pc*P2O$_{RECH158A}$ | |
|---|---|---|---|---|---|---|
| | *β-3F*Glc | | *β-3F*Glc | | *β-3F*Glc | |
| Active-site conformer[b] | Productive 2-oxidation binding mode | | Productive 2-oxidation binding mode | | Productive 2-oxidation binding mode | |
| Sugar–protein interactions[c] | O1 | A546 O | O1 | A551 O | O1 | A551 O |
| | *O2* | *H448 Nε2* | *O2* | *H553 Nε2* | *O2* | *H553 Nε2* |
| | *O2* | *N593 Nδ2* | *O2* | *N596 Nδ2* | *O2* | *N596 Nδ2* |
| | F3 | Q448 Nε2 | F3 | Q454 Nε2 | F3 | Q454 Nε2 |
| | O4 | D452 Oδ2 | O4 | D458 Oδ2 | O4 | D458 Oδ2 |
| | O6 | Y456 Oη | O6 | Y462 Oη | O6 | Y462 Oη |

[a] PDB code 3PL8.
[b] The following three criteria are considered consistent with a productive binding mode: (i) the sugar is oriented for oxidation at C2; (ii) the substrate-binding loop is in the semi-open conformation; (iii) the side chain Oγ1 group of Thr169 is pointing away from the flavin N(5)/O(4) locus.
[c] Italicized interactions represent interactions with the catalytic residues.

(phosphate buffered saline, PBS). The sample was homogenized using AVESTIN Emulsiflex-C3, and the lysate collected in a beaker on ice. The lysate was then centrifuged at 4 °C, (3900 *rcf*) using Avanti J-20 XP centrifuge (Beckman) with rotor JA 25.50 for 30 min to pellet the cell debris.

A 2-mL $Ni^{2+}$-charged immobilized metal affinity chromatography (IMAC) Ni-NTA agarose resin (Invitrogen) was washed and equilibrated with lysis buffer. The clear lysate was passed through the column and the flow through collected, followed by 2 column volumes (CVs) of washing with wash buffer [PBS, 20 mM imidazole] to elute non-specifically binding proteins. *Pc*P2O was eluted with elution buffer [PBS, 500 mM imidazole]. To remove the $His_6$ tag, the protein was incubated at 1:100 ratio with TEV protease in a dialysis bag (molecular weight cut off, MWCO, 12–14 kDa) containing 50 mM Tris, 0.5 mM EDTA and 1 mM dithiothreitol (pH 8.0), and left at 4 °C overnight. Following TEV protease treatment, *Pc*P2O was subjected to a second round of $Ni^{2+}$-IMAC purification, and the flow through containing the untagged protein was collected.

The protein sample was concentrated to 35 mg/mL using a Vivaspin® centrifugal concentrator (MWCO 50 kDa), and further purified by size-exclusion chromatography using a HiLoad™ 16/60 Superdex™ 200 prep grade column (GE Healthcare Life Sciences) equilibrated with 20 mM 4-(2-hydroxyethyl)-1-piperazineethanesulfonic acid (HEPES) pH 7.2, and 150 mM NaCl. Purity of the *Pc*P2O preparation was assessed by SDS–PAGE. Protein fractions were pooled and concentrated to 12 mg/mL using the Vivaspin® centrifugal concentrator (MWCO 50 kDa), and used as stock solution for subsequent crystallization screening and optimization plates.

### 2.3. Crystallization and data collection

The vapor diffusion hanging drop method was used for all *Pc*P2O crystallization experiments, and screening performed using commercially available screens: PACT suite (Qiagen), JCSG+ suite (Qiagen), and Crystal Screen HT (Hampton Research). *Pc*P2O$_{NATWT}$ crystals were of space group $P3_221$ with one homotetramer in the asymmetric unit (asu). The crystals grew from hanging drops mixed by equal volumes of 15 $OD_{280}$/mL protein stock and reservoir containing 0.1 M 2-(*N*-morpholino) ethanesulfonic acid (MES)-OH buffer (pH 5.2), 0.2 M $MgCl_2$, 32% (w/v) polyethylene glycol (PEG) 400. *Pc*P2O$_{RECWT}$ crystals were of space group $P2_1$ (one homotetramer per asu) and grew from drops prepared by equal volumes of 22 mg/mL protein [in 50 mM HEPES (pH 6.5), 150 mM NaCl] and reservoir [containing 0.1 M Tris–HCl (pH 8.5), 0.1 M $MnCl_2$, 30% (w/v) PEG 400]. *Pc*P2O$_{RECH158A}$ crystals belonging to space group $P2_1$ (two homotetramers per asu) were crystallized from equal volumes of a protein stock (13 mg/mL *Pc*P2O in 0.2 M HEPES, pH 7.2) and reservoir solution containing 0.2 M $NH_4Cl$, 15% (w/v) PEG 6000, and 0.1 M HEPES (pH 7.0). All crystals were yellow in color indicating unmodified oxidized enzymes.

The ligand complexes were prepared as followed: the *Pc*P2O$_{RECWT}$ crystal was immersed in a reservoir solution containing *3F*Glc; and the *Pc*P2O$_{RECH158A}$ crystal was briefly exposed to a saturated solution of *3F*Glc dissolved in 0.2 M $NH_4Cl$, 25% (w/v) PEG 6000, 0.1 M HEPES (pH 7.0). All crystals were vitrified in liquid nitrogen prior to data collection. Intensity data were collected at 100 K using synchrotron radiation at beamline *I*911–2 and *I*911–3, MAX-lab (Lund, Sweden), followed by data processing and scaling using the *XDS* package [27]. See Table 2 for crystal and data collection statistics.

### 2.4. Structure determination and refinement

Phasing was performed by molecular replacement using *PHASER* [28] included in the *PHENIX* suite [29] using the refined model of *Tm*P2O variant H167A as starting model (PDB: 3PL8 [18]). For *Pc*P2O$_{NATWT}$ and *Pc*P2O$_{RECWT}$ crystallographic refinement was performed using *PHENIX* initially, and with *REFMAC5* [30] during the later stages of refinement. Refinement included anisotropic scaling, calculated hydrogen scattering from riding hydrogens, and atomic displacement parameter refinement using the translation, libration, screw-rotation (TLS) model. TLS models were built using the TLS Motion Determination server [32]. *Pc*P2O$_{RECWT}$ was refined with *PHENIX* throughout. Individual isotropic temperature factors were refined, and TLS was included in the last refinement round. All model building was done manually using the program O [33] and Coot [34] guided by $\sigma_A$-weighted $2F_o - F_c$ and $F_o - F_c$ electron-density maps. The same sets of $R_{free}$ reflection were used throughout refinement. Missing loop residues due to flexibility and disorder were not modeled, and include for *Pc*P2O$_{NATWT}$, A1–A12, A57–A64, A311–A318, A349–A365, A618–A620, B1–B12, B311–B318, B350–B365, B618–B620, C1–C12, C57–C64, C311–C318, C349–C365, C618–C620, D1–D12, D57–D64, D311–D318, D349–D365, D618–D620; for *Pc*P2O$_{RECWT}$, A1–A12, A57–A65, A310–A318, A349–A365, A618–A620, B1–B9, B58–B65, B310–B318, B349–B365, B618–B620, C1–C12, C310–318, C349–C365, C618–C620, D1–D12, D57–D65, D310–D318, D349–D365, D618–D620; and for *Pc*P2O$_{RECH158A}$, 57–69, 310–318 and 618–620 for all eight monomers A–H in two homotetramers. In addition, the following loop residues are missing: A349–A367, B349–B365, C349–C365, D349–D365, E349–E367, F349–F365, G349–G365 and H349–H365. Model refinement statistics are given in Table 3. All pictures showing structures were made with the program PyMOL [35].

**Table 2**
*Pc*P2O crystal and data collection statistics.

| *Data collection* [a] | | | |
|---|---|---|---|
| Protein variant | *Pc*P2O$_{NATWT}$ | *Pc*P2O$_{RECWT}$/*3F*Glc | *Pc*P2O$_{RECH158A}$/*3F*Glc |
| Source/Vector | Natural source, *P. chrysosporium* | Recombinant, *E. coli*/pET21a(+) | Recombinant, *E. coli*/pNIC28-Bsa4 |
| Cell constants *a*, *b*, *c* (Å); $\beta$ (°) | 164.0, 164.0, 232.5 | 89.5, 166.4, 91.8; 106.41 | 110.1, 167.1, 168.5; 93.98 |
| Space group / mol. per asu | $P3_221/4$ | $P2_1/4$ | $P2_1/8$ |
| Beamline, $\lambda$ (Å) | Max-lab, *I*911-3, 1.0000 | Max-lab, *I*911-3, 1.0000 | Max-lab, *I*911-2, 1.04094 |
| Resolution range, nominal (Å) | 47.43–1.80 (1.90–1.80) | 46.95–1.80 (1.90–1.80) | 48.56–2.40 (2.50–2.40) |
| Unique reflections | 331, 914 (49, 157) | 235, 360 (35, 011) | 233 ,009 (26, 556) |
| Multiplicity | 11.1 (11.2) | 3.8 (3.8) | 4.9 (4.8) |
| Completeness ( %) | 99.9 (99.9) | 99.0 (98.6) | 98.4 (97.4) |
| $\langle I/\sigma I \rangle$ | 17.1 (2.1) | 12.8 (2.3) | 11.9 (1.7) |
| $R_{sym}$ [b] ( %) | 11.9 (200.3) | 11.8 (102.8) | 10.0 (138.3) |
| *CC*(1/2)[c] | 99.9 (76.3) | 99.6 (58.8) | 99.8 (62.6) |

[a] The outer shell statistics of the reflections are given in parentheses. Shells were selected as defined in *XDS* [27] by the user.
[b] $R_{sym} = [\Sigma_{hkl}\ \Sigma_i\ |I - \langle I \rangle| / \Sigma_{hkl}\ \Sigma_i\ |I|]$ x 100%.
[c] *CC*(1/2) = Percentage of correlation between intensities from random half-datasets. Values given represent correlations significant at the 0.1% level [51].

**Table 3**
*Pc*P2O crystallographic refinement statistics.

| *Crystallographic refinement* | | | |
|---|---|---|---|
| Protein variant | *Pc*P2O$_{NATWT}$ | *Pc*P2O$_{RECWT}$/3FGlc | *Pc*P2O$_{RECH158A}$/*3F*Glc |
| Resolution range (Å) | 46.40–1.80 (1.897–1.800) | 44.05–1.80 (1.897–1.800) | 48.56–2.40 (2.478–2.400) |
| Completeness, all % (outer bin) | 99.9 (99.7) | 99.02 (98.62) | 98.41 (97.00) |
| $R_{factor}$ [a]/work reflns, all | 0.153/329,915 | 0.174/233,846 | 0.205/232,946 |
| $R_{free}$/free reflns, all | 0.171/1999 | 0.214/1514 | 0.265/1500 |
| Number of amino-acid residues | 2293 | 2289 | 4620 |
| Number of non-hydrogen atoms | 19,978 | 20,097 | 37,799 |
| Mean *B* (Å$^2$) protein all/mc/sc | 29.3/26.9/31.8 | 21.5/20.0/23.0 | 37.1/36.1/38.1 |
| Mean *B* (Å$^2$) solvent / N°. mol. | 36.0/1562 | 26.9/1644 | 26.3/775 |
| Rmsd bond lengths (Å), angles (°) | 0.025, 2.23 | 0.021, 2.00 | 0.009, 1.24 |
| Ramachandran: favored / allowed ( %) / outliers[b] | 98.1/99.96/1 | 98.0/99.9/3 | 96.2/100.0/1 |
| PDB accession code | 4MIF | 4MIG | 4MIH |

[a] $R_{factor} = \Sigma_{hkl}\ ||F_o| - |F_c|| / \Sigma_{hkl}\ |F_o|$.
[b] As determined by *MolProbity* [52].

## 3. Results

### 3.1. Overall structure of PcP2O

The overall structure of *Pc*P2O is very similar to that of *Tm*P2O (PDB: 1TT0 [22]). A structure-based amino-acid sequence alignment highlights the most important differences (Fig. 1). The main differences include five insertions in *Pc*P2O (boxed regions A–E in Fig. 1), and one major deletion (boxed region F in Fig. 1). The homotetramer is built up from a dimer of dimers where the A–B and C–D subunit pairs form two essential dimers, respectively, each with an extensive intersubunit interface (Fig. 2A). Insertion A in the sequence alignment is a 22-residue segment (residues 51–72) that corresponds to a loop (Fig. 2B) participating in oligomerization by providing intersubunit interactions with the nearby B subunit. This loop is ordered in only one subunit of the two wild-type *Pc*P2O structures, namely subunit B in *Pc*P2O$_{NATWT}$, and subunit C in *Pc*P2O$_{RECWT}$. In other subunits of *Pc*P2O homotetramers there is no interpretable electron density for residues 57–65 in this oligomerization loop. Insertion B comprises eight residues (residues 169–176) of a surface loop with no apparent role in subunit interactions. Insertion C (residues 230–232) provides an additional turn in an $\alpha$-helix in the substrate-binding domain. Insertion D (residues 310–317) and E (residues 353–367) constitute surface-exposed loops that lack interpretable electron density in all subunits, and are therefore assumed to be highly flexible. The region in *Tm*P2O that is deleted in *Pc*P2O (Fig. 1) comprises residues Thr381 to Thr407 (*Tm*P2O numbering), which is part of the "head" domain in *Tm*P2O (Fig. 2B). The function of this domain is unknown but has been noted to have a remarkably flat surface and be rich in threonine and serine residues [22]. The truncation of the head domain in *Pc*P2O effectively removes the $\beta$-hairpin that constitutes the flat surface in *Tm*P2O (Fig. 2B).

### 3.2. Binding of 3-fluorinated glucose

Ligand complexes have been been reported previously for *Tm*P2O [18,36] and *Peniophora* P2O (PDB: 2F5V; [23]). In the case of *Peniophora* P2O, the authors claimed to have captured a complex with the product, 2-keto-D-glucose. However, at closer inspection of the experimental data, the electron density in the active site was better explained by composite binding of two partly occupied binding modes of glucose, i.e., Glc oriented for productive oxidation at C2, and the competing binding mode where Glc is oriented for oxidation at C3 [18]. Ordered high-resolution complexes of these two principal glucose-binding modes have been described in detail for *Tm*P2O (C2-oxidation mode, PDB: 3PL8 [18]; C3-oxidation mode, PDB: 2IGO [36]), and we therefore have limited the structural comparison presented here to *Tm*P2O.

The active sites of *Pc*P2O and *Tm*P2O are highly conserved. Recombinant wild-type *Pc*P2O (Fig. 3A) and H158A *Pc*P2O (Fig. 3B) bind *3F*Glc in the productive 2-oxidation binding mode as observed for the H167A variant of *Tm*P2O (PDB: 3PL8 [18]). The ligand binds identically in all three complexes *Tm*P2O–*3F*Glc, *Pc*P2O$_{RECWT}$–*3F*Glc and *Pc*P2O$_{H158A}$–*3F*Glc (Fig. 3C). Details of protein-ligand interactions are given in Table 1. As defined for the productive 2-oxidation binding mode of $\beta$-D-glucose [18], the substrate-recognition loop is in the semi-open conformation, and the mechanistically important Thr160 (corresponding to Thr169 in *Tm*P2O) points away from the flavin N(5)/O(4) locus.

The only notable difference between the three structures is that


**Fig. 1.** Structure-based amino-acid sequence alignment of *Pc*P2O and *Tm*P2O. Sequence alignment of *Pc*P2O (UniProtKB Q6QWR1) and *Tm*P2O (UniProtKB Q7ZA32). Gray-shaded boxed regions correspond to amino-acid insertions (regions A–E) and deletions (region F). Every tenth residue is marked with a dot. Amino-acid sequence identities are highlighted in blue. The catalytic amino acids (Thr/His/Asn) are marked by red asterisks, and glucose-binding residues in the highly conserved substrate-recognition loop (DAFSYG loop) are denoted by green asterisks. (For interpretation of the references to colour in this figure legend, the reader is referred to the web version of this article.)

Thr160 in *PcP2O*$_{RECWT}$ shows subtle signs of a mixture of two alternative rotamer conformations: i.e., the rotamer observed for the occluded P2O state where the threonine side-chain hydroxyl group hydrogen bonds to the flavin N(5)/O(4) [23]; and the rotamer that points away from the flavin as observed in substrate-bound active-site conformers relevant to the reductive half-reaction [18,36]. This rotamer ambiguity is not present in the redox-suppressed variants of *Pc*P2O (variant H158A) and *Tm*P2O (variant H167A). The rotamer ambiguity in *PcP2O*$_{RECWT}$ is probably due to the higher rate of flavin reduction than in the flavinylation-ligand mutants. Reduced flavin reduction has been shown for the H167A variant of *Tm*P2O [17]. Due to the high catalytic efficiency of recombinant wild-type *Tm*P2O it proved necessary to use the H167A variant in order to obtain crystal complexes with ordered bound 3- and 2-fluorinated glucose [18,36]. Binding of both 2- and 3-fluorinated glucose has been observed for wild-type *Tm*P2O but with a certain degree of disorder resulting in partly occupied states (unpublished results). Importantly, the structure of *Pc*P2O$_{RECWT}$ complex conclusively proves that the binding observed for *3F*Glc in the redox-suppressed mutants of *Tm*P2O and *Pc*P2O is identical and not introduced by the mutation. The reason for the more ordered binding of *3F*Glc to wild-type *Pc*P2O compared to *Tm*P2O is unknown at this point, but may be due to an overall lower flavin-reduction rate of *3F*Glc by wild-type *Pc*P2O.

The only sequence-related differences near the glucose-binding site are Met388 and Ala551 in *Pc*P2O, which correspond to Leu361 and Val546 in *Tm*P2O. Despite these replacements, *3F*Glc assumes an identical conformation, position and protein interactions as in *Tm*P2O. In *Pc*P2O from the natural source without bound substrate, the substrate-recognition loop is in the fully open conformation with Thr160 pointing away from the flavin N(5)/O(4) locus. This conformation represents the unliganded state of P2O, and is most similar to that of the open conformer of *Tm*P2O H167A in complex with 2-fluorinated glucose [36].

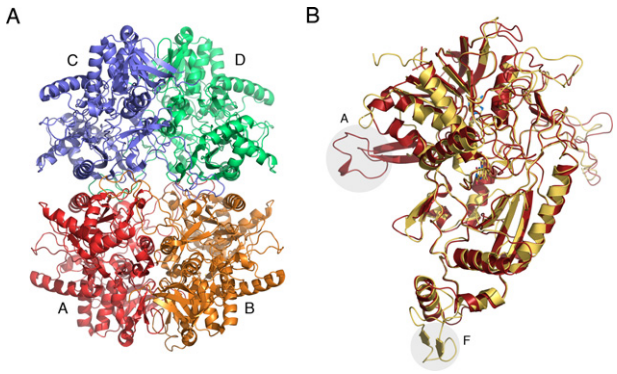


**Fig. 2.** Homotetramer structure and superposition of the monomer structure of *Pc*P2O and *Tm*P2O. (A) The PcP2O homotetramer if formed by two subunit pairs, A/B and C/D, referred to as essential dimers. (B) The subunit structure of $PcP2O_{RECWT}$ (red) overlaid on *Tm*P2O (PDB: 1TT0; yellow). Shaded areas A and F correspond to insertion A in *Pc*P2O and deletion F in *Tm*P2O highlighted in Fig. 1. The FAD cofactor is shown as a ball-and-stick object. (For interpretation of the references to color in this figure legend, the reader is referred to the web version of this article.)

### 3.3. Interactions provided by the N-terminus in the different PcP2O variants

The P2O homotetramer is a dimer of dimers where A/B subunits and C/D subunits form essential dimers with extensive dimer interaction surfaces. The dimers are further assembled into homotetramers, mainly through interactions by the long "oligomerization arms" comprising residues 116–143 in *Tm*P2O [22], and residues 105–134 in *Pc*P2O. According to UniProtKB, the first 9 residues $^{1}$MFLDTTPFR$^{9}$ of the *Pc*P2O amino-acid sequence (UniProtKB Q6QWR1) are annotated as a propeptide sequence (PRO_0000012348). We expressed recombinant wild-type *Pc*P2O and H158A *Pc*P2O in *E. coli* ($PcP2O_{RECWT}$ and $PcP2O_{RECH158A}$) including the putative propeptide in the gene constructs. $PcP2O_{RECWT}$ was cloned into the pET21a(+) vector retaining an additional non-cleavable T7-tag at the N-terminus (before the suggested propeptide sequence), whereas the $PcP2O_{RECH158A}$ variant was cloned into the LIC vector pNIC28-Bsa4 with an N-terminal hexahistidine tag that was subsequently removed by Tobacco Etch Virus (TEV) protease to yield the more authentic N-terminal sequence $^{-1}$SMFLDTTPFR$^{9}$ where the (−1) serine residue is left from the TEV-protease recognition sequence. The precise starting point of the polypeptide chain for *Pc*P2O purified from the natural source is unknown due to the possibility of post-translational modification of the N-terminus such as possible proteolytic maturation cleavage. However, all three *Pc*P2O constructs crystallized in different space groups, which is likely to reflect differences in the primary structure, also for $PcP2O_{NATWT}$.

In the crystal structure of *Pc*P2O from the fungal source ($PcP2O_{NATWT}$), Pro13 is identified as the first residue at the N-terminus of all four subunits of the homotetramer. There is no visible electron density before Pro13 in any of the subunits. This does not mean that the naturally produced enzyme starts at Pro13, only that there is no interpretable electron density for residues 1–12 at the N-terminus. This can be due to removal of the N-terminus (maturation) or high flexibility. In the crystal structure of wild-type $PcP2O_{RECWT}$, the N-terminally positioned T7-tag is forced into the surrounding solvent and not visible in the electron-density map, the first visible residue being Ala10 in subunit B, and Pro13 in subunits A, C and D. The possibility of proteolytic trimming of the N-terminus cannot be excluded, but in this case flexibility due to the N-terminally placed tag is likely.

In the crystal structure of $PcP2O_{RECH158A}$, which has a more authentic N-terminus including the putative propeptide sequence without a leading tag (carrying only an additional serine at the N-terminus), the N-terminus is wedged between the A and B subunits (or C and D subunits) to provide intersubunit interactions at the A/B (or C/D) dimer interfaces of the essential dimer of the 222 tetramer. Residues

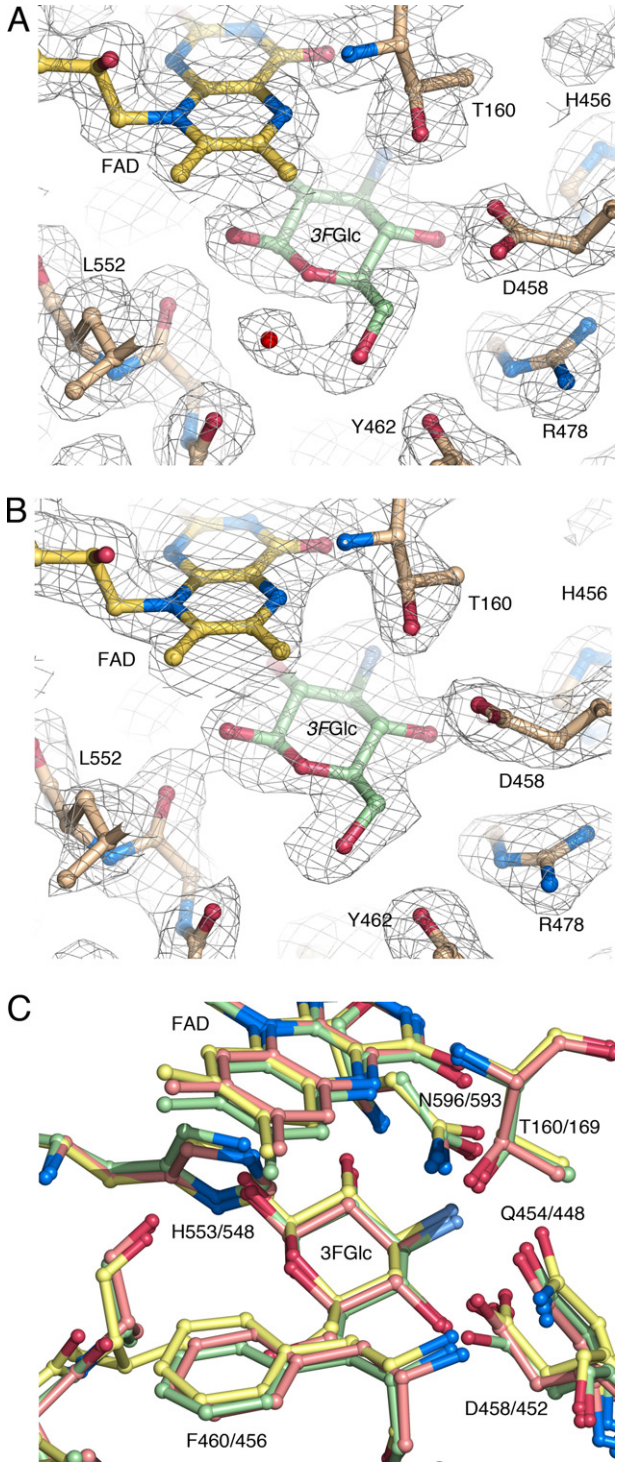


**Fig. 3.** Binding of *3F*Glc to *Pc*P2O. (A) The active site in $PcP2O_{RECWT}$ overlaid with electron density ($\sigma_A$-weighted $2F_o - F_c$) calculated at 1.8 Å resolution and contoured at 1.0$\sigma$. (B) $PcP2O_{RECH158A}$ overlaid with electron density ($\sigma_A$-weighted $2F_o - F_c$) calculated at 2.4 Å resolution and contoured at 1.7$\sigma$. (C) Superposition of the active sites in *Tm*P2O (PDB: 3PL8; yellow), $PcP2O_{RECWT}$ (green) and $PcP2O_{RECH158A}$ (red). The superposition highlights the high agreement of *3F*Glc binding and positioning of critical substrate-binding side chains. Coloring scheme: carbons yellow (*Tm*P2O), green ($PcP2O_{RECWT}$) or red ($PcP2O_{RECH158A}$); oxygen, red; nitrogen, dark blue; fluorine (*3F*Glc), light blue. (For interpretation of the references to colour in this figure legend, the reader is referred to the web version of this article.)

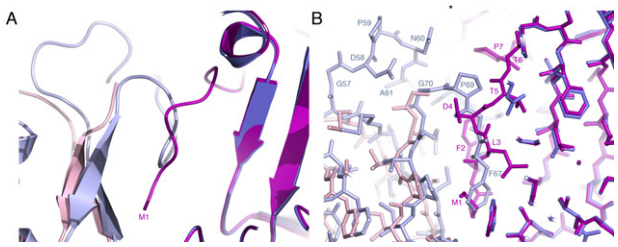


**Fig. 4.** Propeptide interactions at the A/B subunit interface of the *Pc*P2O homotetramer. (A) Superposition of *Pc*P2O$_{NATWT}$ (blue) and *Pc*P2O$_{RECH158A}$ (pink) showing the interface of an essential dimer in the homotetramer. The essential dimer is formed by the A/B or C/D subunit pairs. In the picture, saturated color represents the A subunit and the lighter color the B subunit. Note that the N-terminal sequence in *Pc*P2O$_{RECH158A}$ subunit A has been replaced by a loop of subunit B in *Pc*P2O$_{NATWT}$.. This loop corresponds to insertion A in Fig. 1, and the shaded area A in Fig. 2B. The loop is disordered in *Pc*P2O$_{RECH158A}$. (B) Details of the A/B interface with the same color coding as in panel A and with selected residues highlighted. Met1 (subunit A) in *Pc*P2O$_{RECH158A}$ occupies the same position as Phe67 (subunit B) in *Pc*P2O$_{NATWT}$.. (For interpretation of the references to colour in this figure legend, the reader is referred to the web version of this article.)

1–5 (MFLDT) of the propeptide sequence in subunit A make no interactions with the rest of subunit A, but interact intimately with subunit B at the A/B interface (Fig. 4). Specifically, the sequence $^{2}$FLD$^{4}$ in the propeptide sequence of *Pc*P2O$_{RECH158A}$ subunit A is located between the A and B molecules in the A/B interface of the essential dimer (Fig. 4B). The putative propeptide segment appears to stabilize the 2-fold symmetrical A/B interface by several interactions. Firstly, the N-terminal methionine (Met1) in the propeptide segment of subunit A wedges into the interface to intercalate between, and forming a temporary hydrophobic core together with, Phe50 from both A and B subunits around the 2-fold axis. The propeptide in subunit A offers a limited number possible intra-subunit hydrophobic interactions and hydrogen bonds. However, specific interactions between propeptide A and the neighboring B subunit appear to be limited to a possible hydrogen bond between the backbone amide nitrogen of Phe2 in the putative propeptide segment of subunit A and the side chain O$\gamma$ of Ser52 located at the start of an oligomerization loop in monomer B.

At the A/B interface, the $^{2}$FLD$^{4}$ motif of the putative propeptide in subunit A of *Pc*P2O$_{RECH158A}$ has been replaced by $^{66}$QFG$^{68}$ in the subunit-interface oligomerization loop in subunit B of *Pc*P2O$_{RECWT}$ and *Pc*P2O$_{NATWT}$ (constitutes part of insertion A in Figs. 1 and 2B). In *Pc*P2O$_{RECWT}$, the N-terminal is not visible beyond Pro13. Considering that in *Pc*P2O$_{RECWT}$ the N-terminus cannot be accommodated at the A/B interface because of the T7-tag, this structure may resemble the subunit association mode as it would appear after removal of a propeptide as part of a tentative maturation process. The dynamic character of the putative propeptide and $^{66}$QFG$^{68}$ loop is apparent from the relatively weak density and high temperature factors in *Pc*P2O$_{NATWT}$ and *Pc*P2O$_{RECWT}$. Density for the $^{66}$QFG$^{68}$ loop is missing altogether in *Pc*P2O$_{RECH158A}$. In *Pc*P2O$_{RECH158A}$, the A subunit shows well defined density for the propeptide, whereas the B and E subunits show reasonable density. Subunits D, F and G have weak density for the propeptide and C has poorly defined density. Thus, the subunits in the asymmetric unit show varying degree of disorder indicating that the propeptide is flexible to assume different positions in the individual monomers, resulting in low occupancy. This would be expected considering that the role of the propeptide is to temporarily stabilize the dimer interface and then to be completely displaced upon enzymatic cleavage. A similar behavior is seen for the oligomerization loop (residues 50–70), which has very well-defined density in subunit B of *Pc*P2O$_{RECWT}$ and *Pc*P2O$_{NATWT}$, and considerable flexibility in subunits A, C and D, resulting in non-interpretable electron density.

## 4. Discussion

Despite the low sequence identity of 40%, the overall structure of *Pc*P2O is similar to that of *Tm*P2O. In particular, the active site is structurally highly conserved, which is clearly reflected in similar kinetic behavior [12]. The regioselectivity of C2 *versus* C3 oxidation has been studied in detail for wild-type and mutant *Tm*P2Os with natural and fluorinated substrates using crystal-structure analysis [16,18] and biochemical approaches [14,17]. Binding modes for D-glucose oxidation at C2 [18] and C3 [36] are related by a simple 2-fold rotation of glucose about an axis defined roughly by a line running through a point midway between the atoms C5/O5, and a point midway between atoms C2 and C3. The two orientations in *Tm*P2O are subtly different with nearly identical sets of protein–substrate interactions, however, with two key side-chain interactions (O4–Asp452 O$\delta$2 and O6–Tyr456 O$\eta$) in favor of the 2-oxidation mode [18]. The active-site residues are conserved in *Pc*P2O, including the catalytic His553-Asn596 pair (His548 and Asn593 in *Tm*P2O), and the dynamic substrate-recognition loop (residues 457–467 in *Pc*P2O; 451–461 in *Tm*P2O).

As shown here by the two crystal structure complexes of recombinant *Pc*P2O (wild-type and H158A) with *3F*Glc, the productive binding mode for 2-oxidation of D-glucose is identical to that previously established for *Tm*P2O [18]. Furthermore, the fact that both recombinant wild-type and flavinylation mutant (H158A) bind *3F*Glc identically, proves that the flavinylation *per se* does not significantly alter the structural details of substrate binding. In the case of wild-type *Tm*P2O, *3F*Glc was turned over at an appreciable rate leading to disorder of the ligand in the active site, making it necessary to use a flavinylation mutant (*Tm*P2O H167A) to capture well ordered substrate-binding modes [18,36]. The ordered ligand structure of recombinant wild-type *Pc*P2O with *3F*Glc presented here indicates that turnover might be considerably slower in this case.

In light of the high structural similarity between *Tm*P2O and *Pc*P2O, the difference in melting temperature (17 °C higher for *Pc*P2O) is surprisingly large [21]. The increased thermal stability of *Pc*P2O is likely to be attributed to a large number of subtle differences at the structural level that may not be easily deconvoluted. The general importance of ionic interaction networks for thermal stability of proteins has been recognized and discussed [37–42]. To investigate the possible influence of salt bridges on the different stability of *Pc*P2O and *Tm*P2O, a comparison was made using ESBRI analysis [43]. The result was surprising in that – although *Tm*P2O has a higher total number of salt bridges compared with *Pc*P2O – the ionic links between subunits of the *Tm*P2O homotetramer are very few (PDB: 1TT0 [22]). Only four intersubunit ion links are present out of a total of 247 possible salt bridges (two are formed across the A/B interface, and two across the C/D interface), the rest are intrasubunit ionic interactions. In *Pc*P2O, however, the total number of possible salt bridges is 195, of which 20 are formed between individual subunits across the subunit interfaces (six across the A/C interface, four across the A/D interface, six across the B/D interface, and four across the B/C interface). Thus, the principal determinant likely to contribute to increased thermal stability of *Pc*P2O is the increased number of ionic links formed between subunits of the homotetramer rather than within the subunits.

There is very limited understanding of the functional and structural properties of propeptides, and it is therefore of particular interest to address this question in more detail. Most studies have been concerned with the role of prosegments in the activation of proteases [44]. In the case of redox-active enzymes, one example of interest is lignin peroxidase (LIP; UNP P06181) from *P. chrysosporium*. The enzyme is exported from the hypha *via* the secretory pathway, and contains a 21-residue long N-terminal leader sequence followed by a 7-residue propeptide (PRO_0000023760 [45]). The signal peptide is cleaved after Ala21 [46], and the propeptide is removed by cleavage at a dibasic site after Arg28 [46]. The role of the propeptide in

LIP is not known. Propeptide sequences typically show very low, if any, sequence similarity, and their precise role in folding or activation also differs between different proteins. The possible existence of a propeptide sequence has also been discussed for P2Os. This has been based on the highly heterogeneous N-termini experimentally characterized for various P2Os, although conclusive evidence is still missing [3,15,48].

Based on analysis with SignalP (SignalP 4.1; http://www.cbs.dtu.dk/services/SignalP [50]), the N-terminal sequence of *Pc*P2O is not predicted as a secretion signal, which is expected since P2O is an intracellular protein. Previously observed extracellular release of P2O is most likely through autolysis [10]. Interestingly, it has been reported that the N-terminus of naturally produced *Pc*P2O is susceptible to proteolytic degradation when subjected to cycles of freeze-thawing, and analysis of the proteolytically modified protein by means of LC–MS/MS identified Ala10 as the first amino acid present at the N-terminus [10]. This would be consistent with our *Pc*P2O$_{NATWT}$ structure where the electron density for the N-terminus is visible from Pro13 (due to lack of crystal contacts, $^{10}$ADE$^{12}$ may be flexible). In *Pc*P2O$_{RECWT}$, one subunit indeed shows density from Ala10. Whether the polypeptide chain has been cleaved between Arg9 and Ala10 to eliminate the T7-epitope tag and the following propeptide segment, or whether the tagged N-terminus simply resides flexible in the solvent region is unknown. Regardless, it is evident that in *Pc*P2O$_{NATWT}$ and *Pc*P2O$_{RECWT}$, the N-terminal segment is not placed at the A/B subunit interface where it is found in *Pc*P2O$_{RECH158A}$. In both wild-type structures, the $^{66}$QFG$^{68}$ loop of the neighboring subunit has replaced the N-terminus, which may correspond to the subunit interface architecture of mature *Pc*P2O.

In the case of *Pc*P2O$_{RECH158A}$, a vector and gene construct was used that enable the expression of a more authentic N-terminus. In this construct the entire propeptide is present with an additional serine residue preceding the N-terminal methionine residue. The extra serine is a remnant from the TEV protease recognition sequence and is therefore not possible to eliminate. In the *Pc*P2O$_{RECH158A}$ structure, the N-terminus is favorably wedged at the interface between A and B subunits, placing the N-terminal methionine from each subunit on each side of the 2-fold axis of the essential A/B dimer. The interactions formed by the propeptide in subunit A with the segment defined by residues 50–53 in subunit B of *Pc*P2O$_{H158A}$ are replaced by interactions offered by the $^{66}$QFG$^{68}$ loop in subunit B in *Pc*P2O$_{NATWT}$ and *Pc*P2O$_{RECWT}$. This may indicate that the N-terminal sequence serves as a transient propeptide that nucleates essential interactions between A and B subunits of the essential dimer (or C/D dimers) in the 222 tetramer.

Thus, the N-terminal segment may serve the function of an intramolecular chaperone that stabilizes the A/B interface prior to sequestering the $^{66}$QFG$^{68}$ loop of subunit B to assume its final position and conformation at the A/B interface of the mature enzyme. The propeptide segment does not significantly alter the dimer or homotetramer assembly, suggesting that its ability to pack favorably at the interface is an evolved feature, rather than an artifact. Although the present crystal structures cannot serve as absolute proof for the existence of a propeptide chaperone in *Pc*P2O with a role in folding and/or oligomerization, our results and hypothesis provide a basis for further investigations regarding the putative existence and role of propeptides in oligomeric proteins. Site-directed mutagenesis experiments may provide useful, however, caution must be taken to carefully design variants since any amino-acid replacement or deletion may, directly or indirectly, artifically stabilize or destabilize the subunit interface, or alter the folding/oligomerization pathway, rather than to provide information about inherent intramolecular chaperon activity of the N-terminus in folding and/or oligomerization.

## 5. PDB accession numbers

Coordinates and structure factors are available in the Protein Data Bank database under the following accession numbers: wild-type *Pc*P2O from natural source, PDB: 4MIF; recombinant wild-type *Pc*P2O with *3F*Glc, PDB: 4MIG; and *Pc*P2O H158A with *3F*Glc, PDB: 4MIH.

## Acknowledgements

The authors thank the beamline staff at the MAX II beamlines *I*911–2 and *I*911–3 (MAX-LAB, Lund, Sweden) for assistance during data collection. C.D. and T.-C.T. were supported by grants from the Swedish Research Council VR (VR grants 2008-4045 and 2011-5768). The Austrian Science Fund is acknowledged for support to C.K.P. (FWF grants L210 and P22094) and O.S. (Erwin-Schrödinger Fellowship).

## References

[1] Daniel, G., Volc, J., Kubátová, E. and Nilsson, T. (1992) Ultrastructural and immunocytochemical studies on the $H_2O_2$-producing enzyme pyranose oxidase in *Phanerochaete chrysosporium* grown under liquid culture conditions. Appl. Environ. Micobiol. 58, 3667–3676.
[2] Daniel, G., Volc, J. and Kubátová, E. (1994) Pyranose oxidase, a major source of $H_2O_2$ during wood degradation by *Phanerochaete chrysosporium*, *Trametes versicolor*, and *Oudemansiella mucida*. Appl. Environ. Microbiol. 60, 2524–2532.
[3] Artolozaga, M.J., Kubátová, E., Volc, J. and Kalisz, H.M. (1997) Pyranose 2-oxidase from *Phanerochaete chrysosporium* – further biochemical characterisation. Appl. Microbiol. Biotechnol. 47, 508–514.
[4] Giffhorn, F. (2000) Fungal pyranose oxidases: occurrence, properties and biotechnical applications in carbohydrate chemistry. Appl. Microbiol. Biotechnol. 54, 727–740.
[5] Tasca, F., Timur, S., Ludwig, R., Haltrich, D., Volc, J., Antiochia, R. et al. (2007) Amperometric biosensors for detection of sugars based on the electrical wiring of different pyranose oxidases and pyranose dehydrogenases with osmium redox polymer on graphite electrodes. Electroanalysis 19, 294–302.
[6] Tamaki, T., Ito, T. and Yamaguchi, T. (2007) Immobilization of hydroquinone through a spacer to polymer grafted on carbon black for a high-surface-area biofuel cell electrode. J. Phys. Chem. B 111, 10312–10319.
[7] Janssen, F.W. and Ruelius, H.W. (1968) Carbohydrate oxidase, novel enzyme from *Polyporus obtusus*. II. Specificity and characterization of reaction products. Biochim. Biophys. Acta 167, 501–510.
[8] Ruelius, H.W., Kerwin, R.M. and Janssen, F.W. (1968) Carbohydrate oxidase, a novel enzyme from *Polyporus obtusus*. I. Isolation and purification. Biochim. Biophys. Acta 167, 493–500.
[9] Volc, J. and Eriksson, K.-E. (1988) Pyranose 2-oxidase from *Phanerochaete chrysosporium*. Methods Enzymol. 161, 316–322.
[10] De Koker, T.H., Mozuch, M.D., Cullen, D., Gaskell, J. and Kersten, P.J. (2004) Isolation and purification of pyranose 2-oxidase from *Phanerochaete chrysosporium* and characterization of gene structure and regulation. Appl. Environ. Microbiol. 70, 5794–5800.
[11] Manavalan, A., Adav, S.S. and Sze, S.K. (2011) iTRAQ-based quantitative secretome analysis of *Phanerochaete chrysosporium*. J. Proteom. 75, 642–654.
[12] Pisanelli, I., Kujawa, M., Spadiut, O., Kittl, R., Halada, P., Volc, J. et al. (2009) Pyranose 2-oxidase from *Phanerochaete chrysosporium* – expression in *E. coli* and biochemical characterization. J. Biotechnol. 142, 97–106.
[13] Volc, J., Kubatova, E., Daniel, G. and Prikrylova, V. (1996) Only C2-specific glucose oxidase activity is expressed in ligninolytic cultures of the white rot fungus *Phanerochaete chrysosporium*. Arch. Microbiol. 165, 421–424.
[14] Prongjit, M., Sucharitakul, J., Wongnate, T., Haltrich, D. and Chaiyen, P. (2009) Kinetic mechanism of pyranose 2-oxidase from *Trametes multicolor*. Biochemistry 48, 4170–4180.
[15] Leitner, C., Volc, J. and Haltrich, D. (2001) Purification and characterization of pyranose oxidase from the white rot fungus *Trametes multicolor*. Appl. Environ. Microbiol. 67, 3636–3644.
[16] Freimund, S., Huwig, A., Giffhorn, F. and Köpper, S. (1998) Rare keto-aldoses from enzymatic oxidation: substrates and oxidation products of pyranose 2-oxidase. Chem. Eur. J. 4, 2442–2455.
[17] Sucharitakul, J., Wongnate, T. and Chaiyen, P. (2010) Kinetic isotope effects on the non-covalent flavin mutant protein of pyranose 2-oxidase reveal insights into the flavin reduction mechanism. Biochemistry 49, 3753–3765.
[18] Tan, T.C., Haltrich, D. and Divne, C. (2011) Regioselective control of β-D-glucose oxidation by pyranose 2-oxidase is intimately coupled to conformational degeneracy. J. Mol. Biol. 409, 588–600.
[19] Sucharitakul, J., Prongjit, M., Haltrich, D. and Chaiyen, P. (2008) Detection of a C4a-hydroperoxyflavin intermediate in the reaction of a flavoprotein oxidase. Biochemistry 47, 8490–8495.
[20] Prongjit, M., Sucharitakul, J., Palfey, B.A. and Chaiyen, P. (2013) Oxidation mode of pyranose 2-oxidase is controlled by pH. Biochemistry 52, 1437–1445.
[21] Salaheddin, C., Takakura, Y., Tsunashima, M., Stranzinger, B., Spadiut, O., Yamabhai, M. et al. (2010) Characterisation of recombinant pyranose oxidase from

the cultivated mycorrhizal basidiomycete *Lyophyllum shimeji* (hon-shimeji). Microb. Cell Fact. 9, 57.
[22] Hallberg, B.M., Leitner, C., Haltrich, D. and Divne, C. (2004) Crystal structure of the 270 kDa homotetrameric lignin-degrading enzyme pyranose 2-oxidase. J. Mol. Biol. 341, 781–796.
[23] Bannwarth, M., Heckmann-Pohl, D., Bastian, S., Giffhorn, F. and Schulz, G.E. (2006) Reaction geometry and thermostable variant of pyranose 2-oxidase from the white-rot fungus *Peniophora* sp. Biochemistry 45, 6589–6595.
[24] Johnsrud, S.C. and Eriksson, K.E. (1985) Cross-breeding of selected and mutated homokaryotic strains of *Phanerochaete chrysosporium* K-3 – new cellulase deficient strains with increased ability to degrade lignin. Appl. Microbiol. Biotechnol. 21, 320–327.
[25] Savitsky, P., Bray, J., Cooper, C.D.O., Marsden, B.D., Mahajan, P., Burgess-Brown, N.A. et al. (2010) High-throughput production of human proteins for crystallization: the SGC experience. J. Struct. Biol. 172, 3–13.
[26] Doyle, S.A. (2005) High-throughput cloning for proteomics research. Methods Mol. Biol. 310, 107–113.
[27] Kabsch, W. (1993) Automatic processing of rotation diffraction data from crystals of initially unknown symmetry and cell constants. J. Appl. Crystallogr. 26, 795–800.
[28] McCoy, A.J., Grosse-Kunstleve, R.W., Adams, P.D., Winn, M.D., Storoni, L.C. and Read, R.J. (2007) Phaser crystallographic software. J. Appl. Crystallogr. 40, 658–674.
[29] Adams, P.D., Afonine, P.V., Bunkóczi, G.V., Chen, B., Davis, I.W., Echols, N. et al. (2010) PHENIX: a comprehensive Python-based system for macromolecular structure solution. Acta Crystallogr. D 66, 213–221.
[30] Murshudov, G.N., Vagin, A.A. and Dodson, E.J. (1997) Refinement of macromolecular structures by the maximum-likelihood method. Acta Crystallogr. D 53, 240–255.
[31] Collaborative Computational Project. (1994) The CCP4 suite: programs for protein crystallography. Acta Crystallogr. D 50, 760–763, (Number 4) .
[32] Painter, J. and Merritt, E.A. (2006) Optimal description of a protein structure in terms of multiple groups undergoing TLS motion. Acta Crystallogr. D 62, 439–450.
[33] Jones, T.A., Zou, J.Y., Cowan, S.W. and Kjeldgaard, M. (1991) Improved methods for building protein models in electron density maps and the location of errors in these models. Acta Crystallogr. A 47, 110–119.
[34] Emsley, P. and Cowtan, K. (2004) Coot: model-building tools for molecular graphics. Acta Crystallogr. D 60, 2126–2132.
[35] DeLano, W.L. (2002) The PyMOL Molecular Graphics System. Palo Alto, CA, USA: DeLano Scientific .
[36] Kujawa, M., Ebner, H., Leitner, C., Hallberg, B.M., Prongjit, M., Sucharitakul, J. et al. (2006) Structural basis for substrate binding and regioselective oxidation of monosaccharides at C-3 by pyranose 2-oxidase. J. Biol. Chem. 281, 35104–35115.
[37] Vetriani, C., Maeder, D.L., Tolliday, N., Yip, K.S.P., Stillman, T.J., Britton, K.L. et al. (1998) Protein thermostability above 100°C: A key role for ionic interactions. Proc. Natl. Acad. Sci. USA 95, 12300–12305.
[38] Lebbink, J.H.G., Knapp, S., van der Oost, J., Rice, D., Ladenstein, R. and de Vos, W.M. (1999) Engineering activity and stability of *Thermotoga maritima* glutamate dehydrogenase. II: Construction of a 16-residue ion-pair network at the subunit interface. J. Mol. Biol. 289, 357–369.
[39] Gerk, L.P., Leven, O. and Müller-Hill, B. (2000) Strengthening the dimerisation interface of Lac Repressor increases its thermostability by 40 °C. J. Mol. Biol. 299, 805–812.
[40] Karshikoff, A. and Ladenstein, R. (2001) Ion pairs and the thermotolerance of proteins from hyperthermophiles: a 'traffic rule' for hot roads. Trends Biochem. Sci. 26, 550–556.
[41] Bell, G.S., Russell, R.J.M., Connaris, H., Hough, D.W., Danson, M.J. and Taylor, G.L. (2002) Stepwise adaptations of citrate synthase to survival at life's extremes. Eur. J. Biochem. 269, 6250–6260.
[42] Thomas, A.S. and Elcock, A.H. (2004) Molecular simulations suggest protein salt bridges are uniquely suited to life at high temperatures. J. Am. Chem. Soc. 126, 2208–2214.
[43] Constantini, S., Colonna, G. and Facchiano, A.M. (2008) ESBRI: A web server for evaluating salt bridges in proteins. Bioinformation 3, 137–138.
[44] Shinde, U. and Inouye, M. (1993) Intramolecular chaperons and protein folding. Trends Biochem. Sci. 18, 442–446.
[45] Gold, M.H. and Alic, M. (1993) Molecular biology of the lignin-degrading basidiomycete *Phanerochaete chrysosporium*. Microbiol. Mol. Biol. Rev. 57, 605–622.
[46] Ritch, V.J. Jr, Nipper, T.G., Akileswaran, L., Smith, A.J., Pribnow, D.G. and Gold, M.H. (1991) Lignin peroxidase from the basidiomycete *Phanerochaete chrysosporium* is synthesized as a preproenzyme. Gene 107, 119–126.
[47] De Boer, H.A., Zhang, Y.Z., Collins, C. and Reddy, C.A. (1987) Analysis of nucleotide sequences of two ligninase CDNAs from a white-rot fungus, *Phanerochaete chrysosporium*. Gene 60, 93–102.
[48] Nishimura, I., Okada, K. and Koyama, Y. (1996) Cloning and expression of pyranose oxidase cDNA from *Coriolus versicolor* in *Escherichia coli*. J. Biotechnol. 52, 11–20.
[49] Takakura, Y. and Kuwata, S. (2003) Purification, characterization, and molecular cloning of a pyranose oxidase from the fruit body of the basidiomycete, *Tricholoma matsutake*. Biosci. Biotechnol. Biochem. 67, 2598–2607.
[50] Nordahl Petersen, T, Brunak, S., von Heijne, G. and Nielsen, H. (2011) SignalP 4.0: discriminating signal peptides from transmembrane regions. Nat. Methods 8, 785–786.
[51] Karplus, P.A. and Diederichs, K. (2012) Linking crystallographic model and data quality. Science 336, 1030–1033.
[52] Lovell, S.C., Davis, I.W., Arendall, P.I.W. III, de Bakker, W.B., Word, J.M., Prisant, M.G. et al. (2003) Structure validation by Cα geometry: ϕ, ψ and Cβ deviation. Prot. Struct. Funct. Genet. 50, 437–450.